A. Carducci[1-2], A. Petruccelli[3], A. De Santis[4], Rita de Nardis[1-2], Stefan Wiemer[5] and G. Lavecchia[1-2]

[1]Department of Psychological, Territory and Health Sciences, University of Chieti-Pescara, Italy.

[2]CRUST-Interuniversity Center for 3D Seismotectonics with territorial applications.

[3]Former Swiss Seismological Service, ETH Zurich, now at Leithà Srl – Unipol Group.

[4]INGV–Istituto Nazionale di Geofisica e Vulcanologia, Roma, Italy.

[5]Swiss Seismological Service, ETH Zurich, Switzerland.

Corresponding authors:

Andrea Carducci (andrea.carducci@unich.it);

Antonio Petruccelli (antonio.petruccelli@sed.ethz.ch, now at Leithà Srl – Unipol Group: Antonio.Petruccelli@leitha.eu)

Key Points:

- b-values of kinematic classes are evaluated along depth and related to rheological properties of upper-medium crust in Southern California.
- A_λ, a streamlined kinematic fault parameter that directly depends on rake values, is defined and used to sort kinematic classes and their b-values.
- A regression law is calculated which relates b-values to fault styles, stress, and rheology by A_λ, along different depth ranges.

Abstract

Frequency-magnitude relation of earthquakes from Gutenberg-Richter law is computed in Southern California. A supporting dataset is created, by merging coordinates and magnitudes of relocated earthquakes with kinematic parameters from focal mechanisms. Models of increasing complexity are evaluated to test their dependence on differential stress and kinematics. Parameter b-value is confronted against A , a streamlined version of the kinematic fault parameter, depending on rake values. Multiple regressions of b-values against A at increasing depths are performed, to test the significance of the variation along vertical dimension. A linear equation is finally valued as the most probable model to relate the two parameters.

Plain Language Summary

Relation between the number of earthquakes and their magnitudes, also known as b-value from Gutenberg-Richter law, is calculated in Southern California. Several relations linking b-values to space, faulting style, and stress are considered, each with increasing complexity. Finally, the b-value is confronted with quantification of stress and faulting style called A . Possible equations that could

relate to the two parameters are considered and statistically tested at various depths. The best model to explain the relation is demonstrated to be a straight line.

1. Introduction

Gutenberg-Richter law (Gutenberg & Richter, 1944) is one of the most important equations in statistical seismology: according to it, all seismic events with sizes above magnitude of completeness (Mc), are correctly recorded and follow an exponential distribution. The slope of this distribution in a semi-logarithmic diagram, labeled b-value, can oscillate in different tectonic settings around an approximate range of 0.6-1.4 (Udias, 1999). During foreshock activity, b-value drops are considered potential precursors before strong earthquakes (e.g. Chan et al., 2012; Görgün, 2013; Gulia et al., 2016; Gulia & Wiemer, 2019; Papadopoulos et al., 2010). Furthermore, these oscillations have been associated with changes in stress conditions (Wiemer & Wyss, 2002; Wyss, 1973).

Inverse dependency of b-value with differential stress was demonstrated by Scholz (2015). Besides, Schorlemmer et al. (2005) and Petruccelli et al. (2018) showed that b-values harmonically depend on rake angles from focal mechanisms. Petruccelli et al. (2019a) tested all potential models that relate frequency and size of seismic events, faulting style, and spatiality in terms of degrees of freedom.

An alternative way to express both kinematics and stress is unifying them into a single parameter, that assigns values based on faulting style and differential stress. Simpson (1997) defined A_ϕ or *Andersonian fault parameter*, which quantifies the Anderson (1905) faulting regimes and ϕ, the ratio between main stresses (Angelier, 1979, 1984, 1990) in an area. From a geological perspective, A_ϕ recognizes just three Andersonian styles (normal, transcurrent, reverse), though it is continuous in the [0,3] range depending on ϕ variations.

Shape ratios in stress fields are usually calculated by focal mechanisms inversion, which is computationally complex and requires moment tensors summation (Kostrov, 1974). Kinematic features associated with single focal mechanisms are then merged or lost, depending on their weight in the summation, though this operation potentially influences their frequency-magnitude distribution. Wu et al. (2018) proposed a relation between b-value and A_ϕ in Taiwan, but they respectively computed b-values from earthquakes and A_ϕ from inversion of focal mechanisms. However, this procedure may imply a frequency gap between datasets for b and A_ϕ distributions, which is not easily explainable.

This work introduces a modified version of the Andersonian parameter, A_λ, that preserves individual kinematic features. A proper dataset of focal mechanisms from Southern California is compiled and used to evaluate models relating b-values, kinematics, and physical quantities. We consider equations between differential stress, rheology changes and A_λ and, in particular, a linear relation between b-values and A_λ, which proves to be the most realistic model among tested ones.

The Southern California region is a good case study for systematic analyses of all kinematic groups because its faulting systems have a seismic production with an extreme variety of slip senses. Gerstenberger et al. (2001), Mori & Abercrombie (1997) already considered gradients of frequency-size distributions within crustal depths in Southern California. An elastic-plastic rheology transition between upper and middle crust, which is probably responsible for observed shifts in b-values, was identified in this region at approximately 15 km (e.g. Nazareth & Hauksson, 2004; Petruccelli et al., 2019a; Spada et al., 2013), though it did not consider variations due to kinematic styles or rheological parameters. In the following analyses, a kinematics-based distinction for this rheologic transition will be evaluated.

1. Methods and Data

   (a) A parameter

A_λ is the proposed faulting and stress quantification, which strictly depends on rake angles λ. It is the result of a geometric reduction of the stress cube (Angelier, 1979, 1984, 1990; Simpson, 1997), that flattens it to a hexagon (fig 1a). The central angle in the hexagon is a stress ratio ϕ, which in A_λ is a system of three functions of λ angle ranges, as many as the main tectonic regimes. Thus A_λ can be considered a fast and streamlined version of A_ϕ, because it is directly calculated from individual rakes. Demonstration of A_λ equations is given in Supplementary Material Text S2 (Fig. S1).

Kinematic classes sorted by ranges are converted to A_λ classes, expressing both faulting style and stress ratio. Main classes are:

- Normal (N): $\lambda \in [-\frac{5}{6}\pi; -\frac{\pi}{6}] \Rightarrow\ A_\lambda \in [0; 1]$;
- Strike-Slip (SS): $\lambda \in [-\pi; -\frac{5}{6}\pi) \cup (-\frac{\pi}{6}; \frac{\pi}{6}] \cup (\frac{5}{6}\pi; \pi) \Rightarrow\ A_\lambda \in (1; 2]$;
- Thrust/Reverse (R): $\lambda \in [\frac{\pi}{6}; \frac{5}{6}\pi] \Rightarrow\ A_\lambda \in (2; 3]$,

where each rake and A_λ range is respectively 120° and unit-wide.

In the stress hexagon plot, A_λ is the distance along the semi-perimeter from vertical stress $_z$, while the three sides of the hexagon delimit the three major kinematic fields. However, smaller kinematic classes are allowed, as in fig. 1b, where A_λ classes have 0.5-wide ranges.

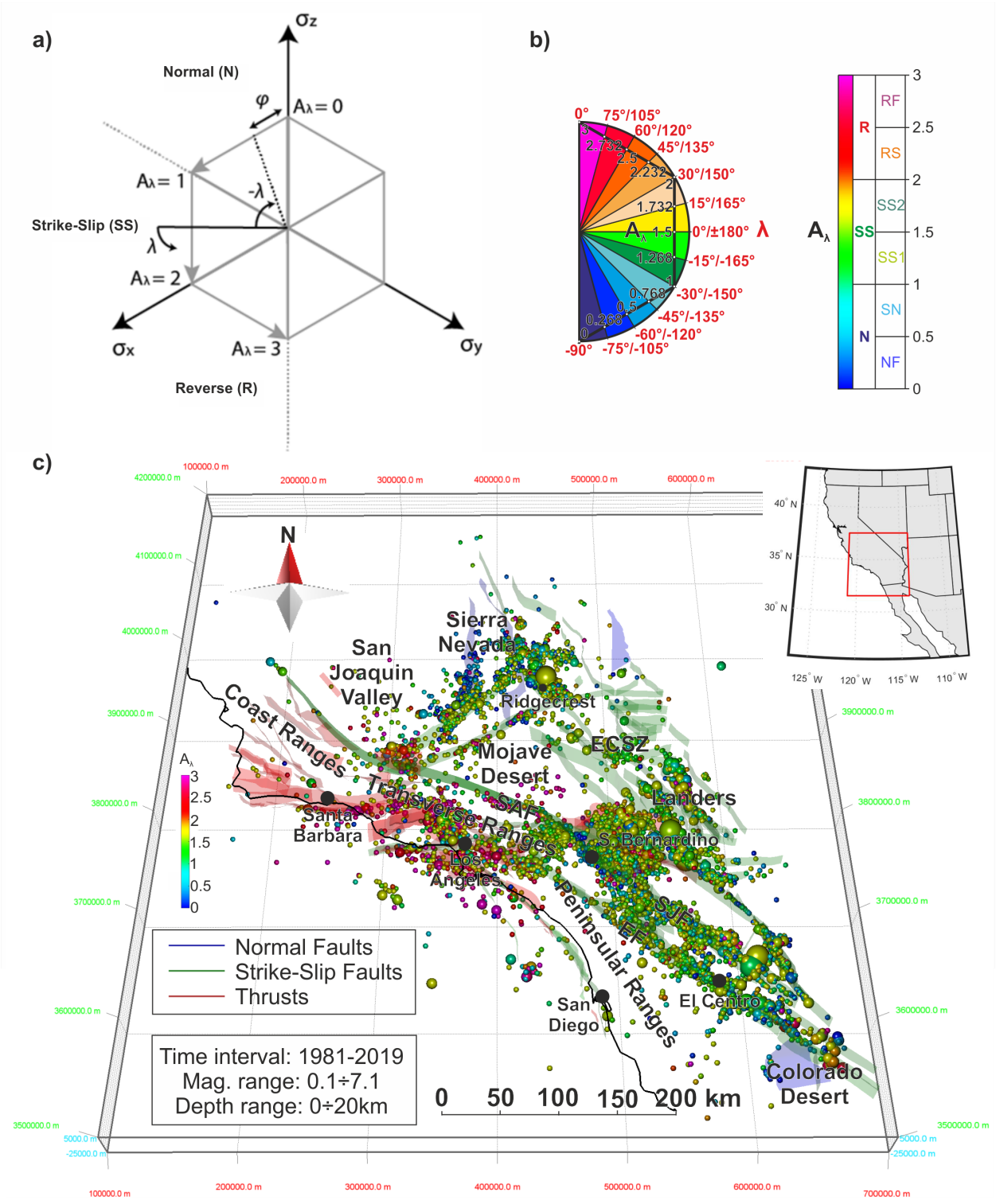
a)
σz
Normal (N)
φ
Aλ = 0
Aλ = 1
-λ
Strike-Slip (SS)
λ
Aλ = 2
σx
Aλ = 3
σy
Reverse (R)
b)
0°
75°/105°
60°/120°
45°/135°
30°/150°
15°/165°
0°/±180°
λ
-15°/-165°
-30°/-150°
-45°/-135°
-60°/-120°
-75°/-105°
-90°
Aλ
R
RF
RS
SS
SS2
SS1
N
SN
NF
c)
N
Sierra Nevada
San Joaquin Valley
Coast Ranges
Ridgecrest
Mojave Desert
ECSZ
Landers
Transverse Ranges
SAF
Santa Barbara
S. Bernardino
Los Angeles
Peninsular Ranges
San Diego
El Centro
Colorado Desert
Normal Faults
Strike-Slip Faults
Thrusts
Time interval: 1981-2019
Mag. range: 0.1÷7.1
Depth range: 0÷20km
0 50 100 150 200 km

Figure 1. A_λ based kinematic analysis of Southern California seismicity from 1981 to 2019 (after Yang et al., 2012). (a) Stress hexagon modified from Simpson (1997) with A_λ ranges for the major kinematic classes (Normal, Strike-Slip, Thrust) (Text S2); (b) half stress hexagon compared with rakes; (c) 3D block diagram of Southern California featuring Community Fault Models v. 5.2, colored by slip senses, and focal mechanisms hypocenters, colored by A_λ values as given in Supplementary File 1.

A_λ kinematic classes are then used as criteria to sort focal mechanisms into subsets. Their b-values are also computed, allowing a direct correlation between the seismic population's frequency and size kinematics and stress ratio.

Fig. 1c shows Yang et al. (2012) focal mechanisms hypocenters, colorized according to the computed A_λ values and superimposed to structures from SCEC Community Fault Model. Most of them are right strike–slip mechanisms and concentrate along the main transcurrent fault systems, such as San Andreas (SAF), East California Shear Zone (ECSZ), San Jacinto (SJF), Elsinore (EF). Nonetheless, distensive A_λ values are also present, clustered around normal dip-slip systems near Ridgecrest in the northern areas, San Bernardino (SBM) in the central sector, and at the southern border with Mexico. Reverse A_λ hypocenters are concentrated around Transverse and Coast Ranges thrusts, in western sectors. Oblique kinematic styles are widespread in most zones due to complex fault interactions.

1. Merged focal mechanisms dataset

The focal mechanisms dataset by Yang & Hauksson (2013) includes 238428 entries for Southern California (magnitude range: -0.3÷7.3; depth range: 0÷35.54 km). In our opinion, vertical relocation is essential to position b-values tightly along depth. Therefore, we merge this dataset with the waveform-relocated earthquake catalog by Hauksson et al. (2012), consisting of 699175 events (magnitude range: -1.02÷7.3; depth range: -2.37÷55.77 km; time range: 1981÷2019) which share ~34% of their identification codes with the focal mechanisms. The resulting Merged Earthquakes-Focal Mechanisms catalog (hereafter MEFM, provided as Supplementary File 1) comprises 237913 entries: their relocated coordinates, vertical uncertainties, and magnitudes derive from the earthquake catalog, while strike, dip, rake, and quality parameters come from focal mechanisms. A_λ-based subsets contain 68419 N, 127501 SS, and 41993 R entries, respectively with magnitudes -0.29÷5.8, -0.17÷7.3, and -0.12÷6.7.

The MEFM dataset is then processed to enhance the overall quality:

- relocation solutions of hypocenters are sorted either by velocity models (1D and 3D) or by the more robust GrowClust algorithm (Trugman & Shearer, 2017) (fig. 2a). Only GrowClust and 3D solutions are used for further analyses; likewise, negative, null, or over 5 km errors are discarded since they are paired with less reliable solutions and statistically negligible (~0.02% of 3D solutions). Over 90% of vertical errors are in the

0÷1 km range, making 1 km-thick sampling windows realistic for analyses. Hypocenters within crustal maximum depths of 20 km are considered.

- Focal mechanisms are provided with four classes of quality (A-B-C-D), according to their azimuthal gaps and mean nodal plane uncertainties. Only solutions from the first two best classes (A-B) are chosen. Still, they comprise only ~56000 entries (~23.5 % of the total).

Magnitude scales are also uniformed to avoid potential bi-linearities (Staudenmaier et al., 2018). Fig. S4 of Supplementary Material reveals that most (~45500) of magnitude scales in merged, B-quality catalog are local, followed by coda duration (~8940), helicorder (~700), and no specified scale (~1350) ones. Ross et al. (2016) conversion from Californian local magnitudes Ml 4 to equivalent moment magnitudes Mw is therefore applied. Other magnitude types and Ml>4 are not affected, since they are mostly aligned with equivalent Mw. All magnitude bins are also uniformed to 0.1 for coherence in calculations. The starting magnitude cutoff is set to 2.2, the most frequent bin (fig. 2b), to prevent incompleteness from small earthquakes.

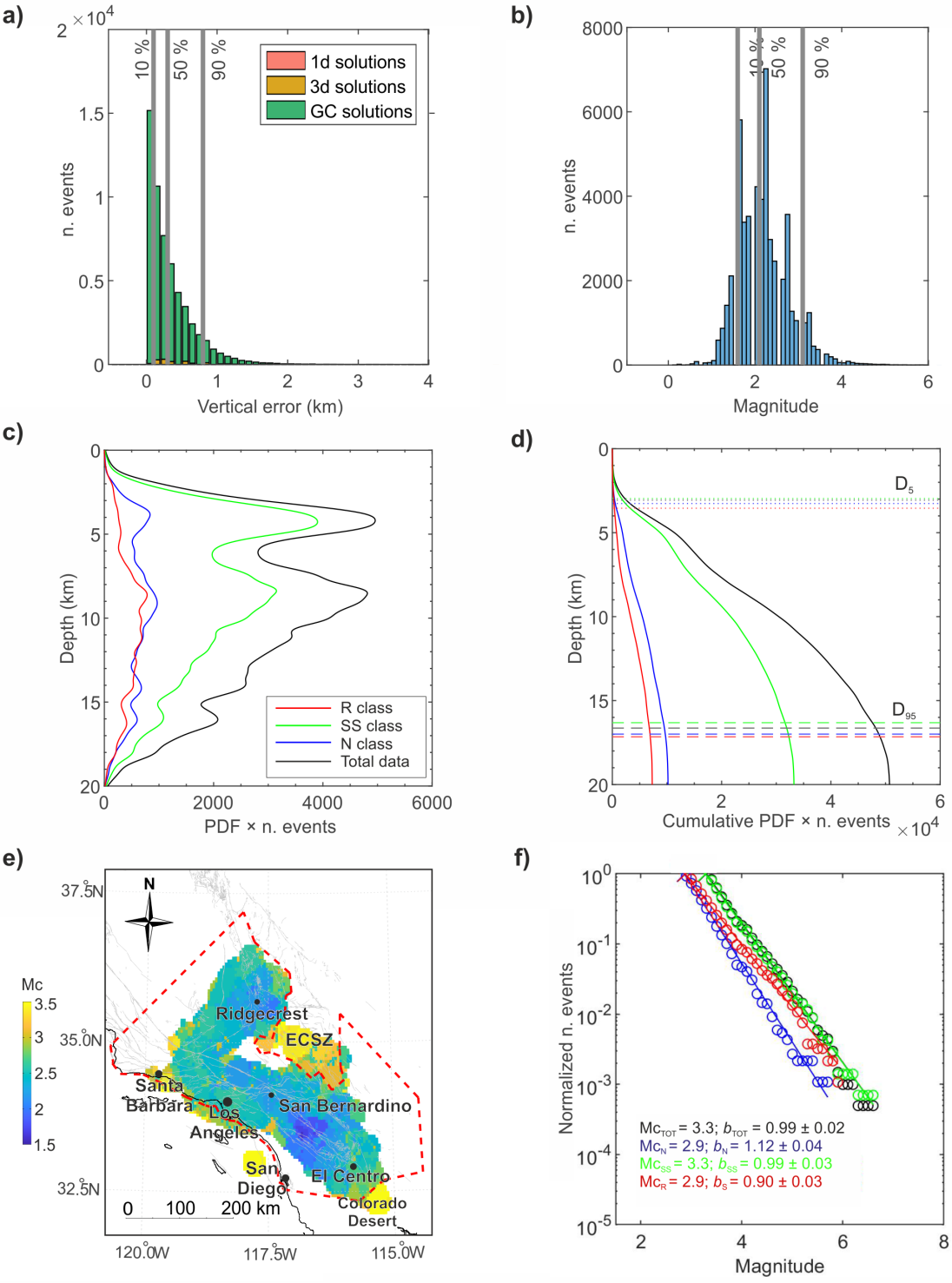
a)
b)
c)
d)
e)
f)
1d solutions
3d solutions
GC solutions
10 %
50 %
90 %
n. events
Vertical error (km)
Magnitude
Depth (km)
PDF × n. events
R class
SS class
N class
Total data
D5
D95
Cumulative PDF × n. events
Mc
Ridgecrest
ECSZ
Santa Barbara
Los Angeles
San Bernardino
San Diego
El Centro
Colorado Desert
0 100 200 km
Normalized n. events
McTOT = 3.3; bTOT = 0.99 ± 0.02
McN = 2.9; bN = 1.12 ± 0.04
McSS = 3.3; bSS = 0.99 ± 0.03
McR = 2.9; bS = 0.90 ± 0.03

Figure 2. Preliminary analyses of MEFM dataset, A-B quality classes, depth bins = 1 km. (a) frequency of vertical errors associated with relocation algorithms; (b) magnitude distribution; (c) probability density functions of hypocenters along their depths per number of total data and per A_λ kinematic classes (N = normal, SS = strike-slip, R = reverse); (d) cumulative version of (c) with D_5 and D_{95} seismic layer boundaries; (e) magnitude of completeness map with selected study area (dashed red line); (f) frequency – magnitude distributions of total data and kinematic classes.

The vertical distribution of hypocenters is also evaluated. In fig. 2c, probability density functions (pdf) of hypocentral depth distributions are multiplied respectively for numbers of total data and of A_λ kinematic classes. Bimodal patterns occur in all pdfs, with a first peak approximately at 4 km of depth. A second peak is found between 8 and 9 km.

Cumulative pdfs for the number of events (fig 2d) are also produced to delimit the seismogenic layer: a shallow boundary of 5% (D_5) of all events starts from ~3 km, while 95 % of events (D_{95}) lay above 16-17 km. D_5 and D_{95} are slightly different among kinematic groups, with a minimum D_5-D_{95} range of 3-16 km for Strike-slip focal mechanisms and a maximum one of 3.5-17 km for Reverse events. These depths are overall compatible with literature (e.g. Nazareth & Hauksson, 2004).

Stacking procedure is finally applied to bypass the choice of the main nodal plane at a regional scale: both nodal planes from each focal mechanism are computed and stacked, so their numbers are doubled (Petruccelli et al., 2018; Petruccelli et al., 2019a).

1. Magnitude of completeness assessment

A map for the magnitude of completeness (Mc) is computed within the Southern California Authoritative Region (fig. 2e): a bi-dimensional grid of 0.05° x 0.05° is assembled to sample from 50 to 750 events, with a maximum searching radius of 25 km. Following the Maximum Curvature method (Woessner & Wiemer, 2005), Mc associated with each node is the most frequent magnitude bin added by 0.2.

From the map, a higher completeness threshold (Mc>3.5) is assessed in nodes from Eastern California Shear Zone, southern borders with Mexico, and offshore areas. Consequently, these points are discarded to guarantee low completeness levels in the study area.

In depth and regression diagrams, Mc is conversely assessed by a modified *b*-stability method (Woessner & Wiemer, 2005): completeness is achieved where all potential *b*-values reach a plateau, in a magnitude range between most frequent and highest values. The minimum sampling number is set to 200 events. This method produces conservative but dynamic Mc values, which are proper for depth analyses; given the initial cutoff cited in paragraph 2.2 and the map boundaries, Mc oscillates within 2.2÷3.5 range.

1. **Crustal Rheology**

Changes in b-values from shifts in physical properties within crustal depths are known since Gerstenberger et al. (2001), Spada et al. (2013), Petruccelli et al. (2019b). We deem that a proper correlation between b-values and differential stress is inescapable from rheological profiles for the upper-middle crust.

Differential stress equations under elastic and plastic rheologies are mentioned in Supplementary Text S4. Critical values within plastic conditions are mainly controlled by strain rate $\dot{\varepsilon}$. Nonetheless, there is no unanimous consensus on the $\dot{\varepsilon}$ value for Southern California crust: $\dot{\varepsilon} = 10^{-12}s^{-1}$ is accepted by some authors (e.g., Shebalin & Narteau, 2017), while $\dot{\varepsilon} = 10^{-14}s^{-1}$ is hypothesized by petrographic analyses in Behr & Hirth (2014). Low $\dot{\varepsilon}$ values generally imply small critical differential stresses and thus reduce the depths for elastic-plastic transition.

Rheological profiles in this work will then consider three possible strain rates ($\dot{\varepsilon_1} = 10^{-12}\ s^{-1}$, $\dot{\varepsilon_2} = 10^{-13}$, $\dot{\varepsilon_3} = 10^{-14}s^{-1}$). Furthermore, elastic-plastic transitions will be plotted as depth layers, since they are not abrupt according to profiles. Rheologic shifts should be identified for each A_λ class because rakes affect critical differential stresses under elastic conditions, so layers are potentially variable for each kinematic class.

1. Kinematic and dynamic-control on b-value

   (a) b-value distributions

Maximum Likelihood approach (Aki, 1965; Bender, 1983; Utsu, 1965) is applied to compute b-values; uncertainties of magnitudes of completeness and b-values are evaluated using the bootstrap method, i.e., standard deviations of results from 500 random samplings.

We first compute frequency–magnitude distributions considering just dependence on faulting style, from the whole dataset and the A_λ-based N, SS, and R kinematic classes subsets, normalized by respective numbers of data (fig. 2f). Results assess that $b_N > b_{SS} > b_R$: this simple model is coherent with previous observations from Gulia & Wiemer (2010) and Petruccelli et al. (2019a).

The second evaluated model is:

$$b(z) = b_0 - k_{\text{kin}} \bullet z \tag{1}$$

where *b(z)* is a decreasing gradient along depth z, from starting value b_0, k_{kin} is a slope depending on kinematic class (Petruccelli et al., 2019a).

Rheological profiles for the whole catalog and kinematic classes, as described in paragraph 2.4., are outlined in fig. 3a. Computed b–values down to 20 km are

plotted in fig. 3b-c and compared to 3a, to determine which strain rate is more compatible with observed b-values.

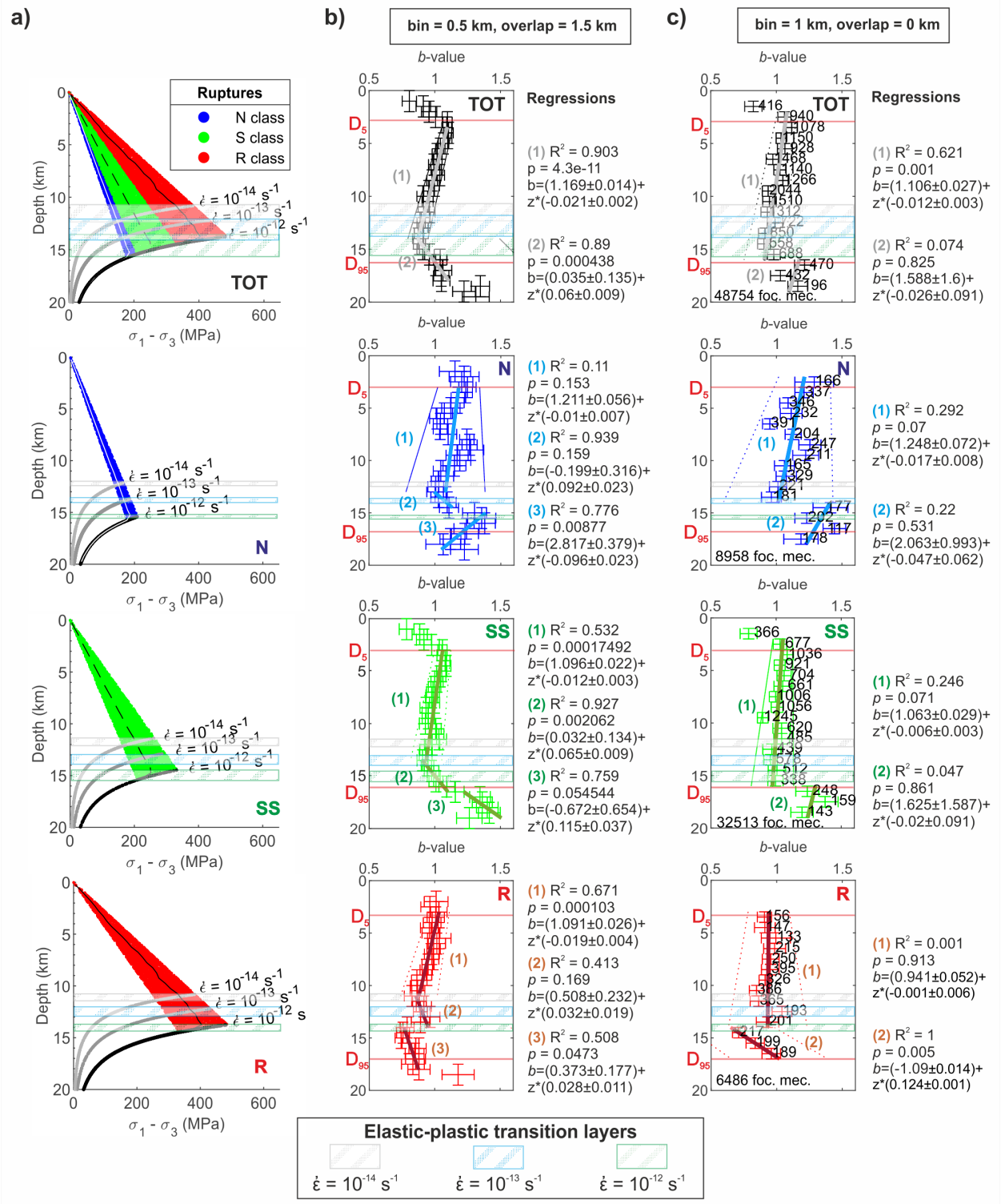
a)
b)
c)
bin = 0.5 km, overlap = 1.5 km
bin = 1 km, overlap = 0 km
Ruptures
N class
S class
R class
TOT
N
SS
R
Depth (km)
σ1 - σ3 (MPa)
b-value
Regressions
(1) R² = 0.903
p = 4.3e-11
b=(1.169±0.014)+
z*(-0.021±0.002)
(2) R² = 0.89
p = 0.000438
b=(0.035±0.135)+
z*(0.06±0.009)
(1) R² = 0.621
p = 0.001
b=(1.106±0.027)+
z*(-0.012±0.003)
(2) R² = 0.074
p = 0.825
b=(1.588±1.6)+
z*(-0.026±0.091)
48754 foc. mec.
(1) R² = 0.11
p = 0.153
b=(1.211±0.056)+
z*(-0.01±0.007)
(2) R² = 0.939
p = 0.159
b=(-0.199±0.316)+
z*(0.092±0.023)
(3) R² = 0.776
p = 0.00877
b=(2.817±0.379)+
z*(-0.096±0.023)
(1) R² = 0.292
p = 0.07
b=(1.248±0.072)+
z*(-0.017±0.008)
(2) R² = 0.22
p = 0.531
b=(2.063±0.993)+
z*(-0.047±0.062)
8958 foc. mec.
(1) R² = 0.532
p = 0.00017492
b=(1.096±0.022)+
z*(-0.012±0.003)
(2) R² = 0.927
p = 0.002062
b=(0.032±0.134)+
z*(0.065±0.009)
(3) R² = 0.759
p = 0.054544
b=(-0.672±0.654)+
z*(0.115±0.037)
(1) R² = 0.246
p = 0.071
b=(1.063±0.029)+
z*(-0.006±0.003)
(2) R² = 0.047
p = 0.861
b=(1.625±1.587)+
z*(-0.02±0.091)
32513 foc. mec.
(1) R² = 0.671
p = 0.000103
b=(1.091±0.026)+
z*(-0.019±0.004)
(2) R² = 0.413
p = 0.169
b=(0.508±0.232)+
z*(0.032±0.019)
(3) R² = 0.508
p = 0.0473
b=(0.373±0.177)+
z*(0.028±0.011)
(1) R² = 0.001
p = 0.913
b=(0.941±0.052)+
z*(-0.001±0.006)
(2) R² = 1
p = 0.005
b=(-1.09±0.014)+
z*(0.124±0.001)
6486 foc. mec.
Elastic-plastic transition layers

Figure 3. *b*-values along depth distributions in Southern California and relation with rheological stratification: (a) rheological profile from differential stress $\sigma_1 - \sigma_3$ against depth, for all focal mechanisms (black), Normal (blue), Strike-Slip (green), and Reverse (red) classes. (b) *b*-values against depth of total data (upper) and kinematic classes, sampling step = 0.5 km, overlapping = 1.5 km. (c) same as (b), but sampling step = 1 km, overlapping = 0 km, sampling number at each depth is indicated. Identified linear regressions are numbered in (b) and (c). D_5 and D_{95} are upper and lower seismogenic layer boundaries according to kinematic classes. Elastic-plastic crustal transition layers depending on strain rates are plotted for all sub-figures.

b-values are calculated by mobile sampling windows, moving vertically by chosen step and overlap. In figure 3b, smoothness is emphasized at the expense of relocation accuracy: windows step and bin are 0.5 km, while overlap is 1.5 km. In contrast, fig. 3c has a larger step and bin of 1 km but no overlap, hence vertical relocation is prominent against smoothness.

Linear regressions in fig. 3b-c, and their R^2 and p significance parameters, are computed and numbered within selected depth boundaries, using Norm L1 regression (see Supplementary Material fig. S15).

Depths above D_5 are generally unreliable: while overlapped total data and SS group distributions increase, no-overlap graphs sketch sparser data and suggest that an over-smoothing effect is happening in the first instance. The lack of data entries for N and R classes supports this hypothesis.

Total data show good regression parameters in the first, descending gradient ($R^2 = 0.903$ and 0.621, $p < 0.01$ and $p = 0.001$, respectively for overlapping and no-overlap distributions); a second, rising gradient starts within depth levels associated to $\dot{\varepsilon}_3$ and outlines very good parameters ($R^2 = 0.89$, $p < 0.01$) but is only visible for overlapping distribution, while a noticeable step in *b* levels is present in no-overlap one at D_{95} level. No recognizable regression is found after $D_{95.}$

In N group, the first descending gradient is recognized between D_5 and ~13-14 km, but regression parameters are not very significant ($R^2 = 0.11 \div 0.292$, $p = 0.153 \div 0.07$ respectively for overlapping and no-overlap ones). *b*-values abruptly rise before the $\dot{\varepsilon}_3$ depth levels when overlap is applied, with uncertain regression parameters ($R^2 = 0.939$, $p = 0.159$). This regression, however, is not present in no-overlap distribution, and a gap is visible at $\dot{\varepsilon}_2$ transition depths. A second, descending gradient shows variable significance ($R^2 = 0.776$ and 0.22, $p < 0.01$ and $= 0.531$) and starts after $\dot{\varepsilon}_3$ and $\dot{\varepsilon}_2$ transitions, depending on overlap presence.

SS class and total focal mechanisms share similar behaviors. Although, the first descending gradient has mediocre linearity ($R^2 = 0.532$ and 0.246, $p < 0.01$ and $p = 0.071$). Once again, *b*-values are rising at $\dot{\varepsilon}_3$ transition with overlap, in the second case a gap is present. After $D_{95,}$ values become inconsistent, since

both increasing and decreasing gradients appear respectively in overlap and no-overlap cases.

R class is similar to SS one when windows overlap, with descending gradient down to ~ 11 km and good linearity ($R^2 = 0.671$, $p < 0.01$) followed by rising values down to $\dot{\varepsilon}_3$ depths, with worse parameters ($R^2 = 0.413$, $p = 0.169$). Without overlap, linearity is not significant ($R^2 = 0.001$, $p = 0.913$) and rising b-values before transition depths are not displayed. Nonetheless, in both cases a gap is visible at transition levels, followed by lower b-values, which then grow from transition depths down to D_{95}: with overlap $R^2 = 0.508$ and $p = 0.0473$, without overlap, $R^2 = 1$ and $p = 0.005$, though based on very sparse data entries.

1. b–A regression models

An alternative model is investigated, based on b-A_λ relation. Focal mechanisms are binned into mobile windows based on associated A_λ values, moving by steps = 0.25, with bins = ± 0.125 and null overlaps, and their b-values computed. Coherently with hypocenters distribution peaks (fig. 2c) and D_5-D_{95} limits (fig. 2d), we analyze five depth ranges: 0-3, 3-7, 7 – 10, 10-15 km, 15-20 km.

Within these depth ranges, differential stresses of focal mechanisms are calculated using equations in Supplementary Text S4 and compared to their associated A_λ values. Results are shown in Supplementary Fig. S16.

Second-order Akaike Information Criterion (Akaike, 1974; Cavanaugh, 1997) is employed as a goodness-of-fit test: the lowest scoring model is considered the best fitting one, with a penalty for over-complexity. The competing models are plotted in fig 4a:

1. linear model: $b\left(A_\lambda\right) = b_\lambda - k_\lambda A_\lambda$.
2. 3rd-grade polynomial: $b\left(A_\lambda\right) = p_1 {A_\lambda}^3 + p_2 {A_\lambda}^2 + p_3 A_\lambda + p_4$.
3. 7th-grade polynomial, purposedly chosen as a complex but possible model: $b\left(A_\lambda\right) = p_1 {A_\lambda}^7 + p_2 {A_\lambda}^6 + ... \, p_7 A_\lambda + p_8$.
4. Sum of sines and cosines, thus a harmonic function derived from Fourier series: $b\left(A_\lambda\right) = p_1 \sin\left(3A_\lambda\right) + p_2 \cos\left(3A_\lambda\right) + p_3 \sin\left(2A_\lambda\right) + p_4 \cos\left(2A_\lambda\right) + p_5 \sin\left(A_\lambda\right) + p_6 \cos\left(A_\lambda\right) + p_7$.
5. Another possible sum of sines and cosines: $b\left(A_\lambda\right) = p_1 \sin\left(3wA_\lambda\right) + p_2 \sin\left(2wA_\lambda\right) + p_3 \cos\left(2wA_\lambda\right) + p_4 \sin\left(wA_\lambda\right) + p_5 \cos\left(wA_\lambda\right) + p_6$.

Results are shown in fig. 4a and Supplementary File 1.

AICc score of model 1 is the lowest in the 3-7 km and 10-15 km ranges; between 7 and 10 km, its result is slightly worse than model 2, although this is likely due to fluctuations in b-value of single A_λ groups; besides, the difference is minimal (-28.2764 against -28.7596).

Slopes and intercepts in model 1 regression remain overall stable along the vertical dimension. Exceptions are scattered entries at <3 km due to low sampling

values, which make this layer unreliable.

Besides, model 1 performs worse than the second one in the 15-20 km range, where rheology transition occurs, though the score in model 1 is still better than in models 3-4-5. It is then quite safe to assume that model 1 is reliable only within upper crustal depths.

Mean and standard deviations of slope and intercept for model 1 within the 3-15 km range are calculated, giving the following parameters:

$$b\left(A_\lambda\right) = b_\lambda - k_\lambda A_\lambda = (1.1533 \pm 0.0208) + (-\ 0.1033 \pm 0.0153) \bullet A_\lambda$$

(2)

b vs A_λ results are also implemented into a 3D figure (fig. 4b), using depth steps of 3 km. Finally, point data are interpolated by Lowess smoothing surfaces to visualize the constancy along vertical.

We calculate the ratio between slopes in (2) in the 3-15 km range and in Scholz (2015):

$$k_\lambda^{'} = \frac{k_\sigma}{k_\lambda} = \frac{-0.0012 \pm 0.0003}{-0.1033 \pm 0.0153} \cong 0.012 \pm 0.003$$

(3)

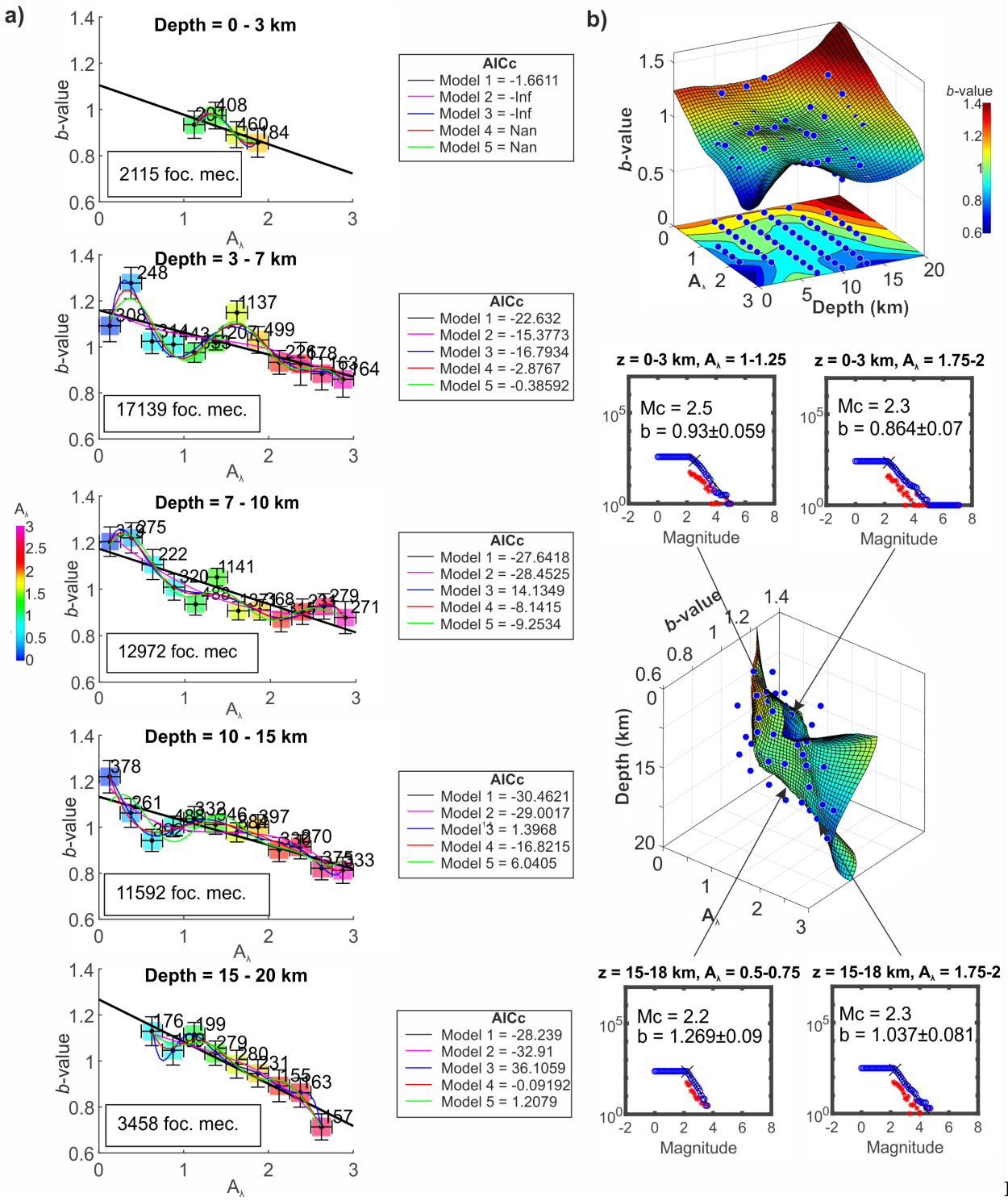
a)
Depth = 0 - 3 km
2115 foc. mec.
AICc
Model 1 = -1.6611
Model 2 = -Inf
Model 3 = -Inf
Model 4 = Nan
Model 5 = Nan
Depth = 3 - 7 km
17139 foc. mec.
AICc
Model 1 = -22.632
Model 2 = -15.3773
Model 3 = -16.7934
Model 4 = -2.8767
Model 5 = -0.38592
Depth = 7 - 10 km
12972 foc. mec
AICc
Model 1 = -27.6418
Model 2 = -28.4525
Model 3 = 14.1349
Model 4 = -8.1415
Model 5 = -9.2534
Depth = 10 - 15 km
11592 foc. mec.
AICc
Model 1 = -30.4621
Model 2 = -29.0017
Model 3 = 1.3968
Model 4 = -16.8215
Model 5 = 6.0405
Depth = 15 - 20 km
3458 foc. mec.
AICc
Model 1 = -28.239
Model 2 = -32.91
Model 3 = 36.1059
Model 4 = -0.09192
Model 5 = 1.2079
b-value
A
b)
b-value
Depth (km)
z = 0-3 km, A = 1-1.25
Mc = 2.5
b = 0.93±0.059
z = 0-3 km, A = 1.75-2
Mc = 2.3
b = 0.864±0.07
Magnitude
z = 15-18 km, A = 0.5-0.75
Mc = 2.2
b = 1.269±0.09
z = 15-18 km, A = 1.75-2
Mc = 2.3
b = 1.037±0.081

Fi

4. Computed 2d and 3d b-value regressions models from the MEFM dataset. (a) linear to sinusoidal regressions at selected depth ranges of b-values against A_λ kinematic classes (b) (up) Lowess smoothing surface of b-values against A_λ groups at sliding depth windows (step = 3 km); (down) same as (up), but the depth axis is vertical. Sample frequency-magnitude distributions for shallow and high depths, low and high A_λ values are displayed.

1. Discussion and Conclusions

Gradients of b-values along depth by kinematic groups of the MEFM dataset are unstable, but they generally decrease within linear rheology limits in each A_λ class as seen in literature (e.g. Petruccelli et al., 2019a; Staudenmaier et al., 2019). For less frequent kinematics, N and R, we hypothesize that in Southern California their b-value depth distributions are expressions of specific seismogenic structures, rather than regional trends since their hypocenters are more localized. Anyway, even the SS group, which numbers the most frequent and distributed kinematics, shows minor fluctuations along the depth. These fluctuations are also unrelated to the number of sampled events and may be caused by minor rheologic transitions.

Fluctuations of b-values above the D_5 seismogenic boundary are probably linked to various factors, such as relocation bias for events that are proximal to recording seismic networks, low amount of data, and pore pressure variations along Southern California upper crustal depths (Shebalin and Narteau, 2017).

On the other hand, in the proximity of D_{95}, a rheologic transition between 16 and 17 km, compatible with an approximate strain rate value of $\dot{\varepsilon} = 10^{-12} s^{-1}$, seems plausible according to b-values of kinematic classes at higher depths. Variations above these depths are likely associated with this transition, though overlaps play a significant role here. From analyses of not-overlapping b distributions, we suggest a more abrupt passage than what was previously hypothesized, and secondly, this transition slightly fluctuates among A_λ classes.

Conclusive results on the b distributions under the rheologic transition are not available, due to a lack of data for calculations under the D_{95} boundary. b-values show a sudden rising at approximately D_{95} depth, then follow lowering gradients depending on kinematic classes. An exception is the R class, which drops and then displays a rising gradient.

Regarding the relation between b and A_λ, the goodness-of-fit test shows that a linear model is dominant at most depths. Exceptions are due to already mentioned b-values at shallow depths or instability in single kinematic classes (especially N group, at 7 – 10 km range). At depths where the linear model is prevalent, parameters are mostly stable along with depth, with acceptable R^2 correlation coefficients (generally > 0.7).

Wu et al. (2018) findings for the Taiwan area also suggest that a linear model between b-values and quantified differential stresses and kinematics is globally valid with some regional variations given that their parameters are similar to

the ones in equation (2). Differences in results may also be due to their methodologies and to our equation being limited to the 3-15 km depth range, but other studies under different tectonic settings and methodologies would settle the matter.

Our findings are also compatible with Scholz's (2015) observations considering that a strong inverse correlation between differential stress and b-values is outlined. Differential stresses in fig. 3a and Supplementary Fig. S16 are computed using Model 3.1 from Petruccelli et al. (2019a). Similar behavior in b-values and differential stresses at the respective depth ranges is evidence that differential stress is directly involved in b-values vs. kinematics equations and that Model 3.1 might be a realistic explanator.

These observations may be another step towards a physical understanding of the b-value inside the earthquake process. However, numerical modeling and parametrization are still some of the main obstacles in the use of frequency-size distributions for seismic hazard assessment and there is more room for improvements.

Data Sources

For the original focal mechanisms and earthquakes catalogs used in this work, visit respectively (https://scedc.caltech.edu/data/alt-2011-yang-hauksson-shearer.html and https://scedc.caltech.edu/data/alt-2011-dd-hauksson-yang-shearer.html).

Southern California Community Fault Model is available for download at https://www.scec.org/research/cfm.

Southern California Authoritative Region polygon boundaries can be found at http://www.ncedc.org/anss/archived-anss-information.html.

Acknowledgments

We thank prof. E. Hauksson for the feedback he has given on the datasets. Angelo de Santis thanks ASI for funding Limadou-Science+ Project. We also thank EEH Ph.D. Course (Prof. G. Lavecchia coordinator) for financing and supporting the research.

References

Akaike, H. (1974). A new look at the statistical model identification. *IEEE Transactions on Automatic Control*, *19*(6), 716–723. https://doi.org/10.1109/TAC.1974.1100705Aki, K. (1965). Maximum likelihood estimate of b in the formula logN = a − bM and its confidence limits. *Bulletin of Earthquake Research*, *43*, 237–239. https://doi.org/https://doi.org/10.15083/0000033631Anderson, E. M. (1905). The dynamics of faulting. *Transactions of the Edinburgh Geological Society*, *8*(3), 387–402. https://doi.org/10.1144/transed.8.3.387Angelier, J. (1979). Determination of the mean principal directions of stresses for a given fault population. *Tectonophysics*, *56*(3–4), T17–T26. https://doi.org/10.1016/0040-1951(79)90081-7Angelier, J. (1984). Tectonic analysis of fault slip data

sets. *Journal of Geophysical Research: Solid Earth*, *89*(B7), 5835–5848. https://doi.org/10.1029/JB089iB07p05835Angelier, J. (1990). Inversion of field data in fault tectonics to obtain the regional stress-III. A new rapid direct inversion method by analytical means. *Geophysical Journal International*, *103*(2), 363–376. https://doi.org/10.1111/j.1365-246X.1990.tb01777.xBehr, W. M., & Hirth, G. (2014). Rheological properties of the mantle lid beneath the Mojave region in southern California. *Earth and Planetary Science Letters*, *393*, 60–72. https://doi.org/10.1016/j.epsl.2014.02.039Bender, B. (1983). Maximum likelihood estimation of b values for magnitude grouped data. *Bulletin of the Seismological Society of America*, *73*(3), 831–851. https://doi.org/10.1785/BSSA0730030831Cavanaugh, J. E. (1997). Unifying the derivations for the Akaike and corrected Akaike information criteria. *Statistics & Probability Letters*, *33*(2), 201–208. https://doi.org/10.1016/S0167-7152(96)00128-9Chan, C.-H., Wu, Y.-M., Tseng, T.-L., Lin, T.-L., & Chen, C.-C. (2012). Spatial and temporal evolution of b-values before large earthquakes in Taiwan. *Tectonophysics*, *532–535*, 215–222. https://doi.org/10.1016/j.tecto.2012.02.004Gerstenberger, M., Wiemer, S., & Giardini, D. (2001). A systematic test of the hypothesis that the b value varies with depth in California. *Geophysical Research Letters*, *28*(1), 57–60. https://doi.org/10.1029/2000GL012026Görgün, E. (2013). Analysis of the b-values before and after the 23 October 2011 Mw 7.2 Van–Erciş, Turkey earthquake. *Tectonophysics*, *603*(October 2011), 213–221. https://doi.org/10.1016/j.tecto.2013.05.030Gulia, L., & Wiemer, S. (2010). The influence of tectonic regimes on the earthquake size distribution: A case study for Italy. *Geophysical Research Letters*, *37*(10), n/a-n/a. https://doi.org/10.1029/2010GL043066Gulia, L., & Wiemer, S. (2019). Real-time discrimination of earthquake foreshocks and aftershocks. *Nature*, *574*(7777), 193–199. https://doi.org/10.1038/s41586-019-1606-4Gulia, L., Tormann, T., Wiemer, S., Herrmann, M., & Seif, S. (2016). Short-term probabilistic earthquake risk assessment considering time-dependent b values (Vol. 43, pp. 1100–1108). https://doi.org/10.1002/2015GL066686Gutenberg, B., & Richter, C. F. (1944). Frequency of earthquakes in California*. *Bulletin of the Seismological Society of America*, *34*(4), 185–188. https://doi.org/10.1785/BSSA0340040185Hauksson, E., Yang, W., & Shearer, P. M. (2012). Waveform Relocated Earthquake Catalog for Southern California (1981 to June 2011). *Bulletin of the Seismological Society of America*, *102*(5), 2239–2244. https://doi.org/10.1785/0120120010Kostrov, V. V. (1974). Seismic moment and energy of earthquakes, and seismic flow of rock. *Izv. Acad. Sci. USSR, Phys. Solid Earth*, *1*, 23–40.Mori, J., & Abercrombie, R. E. (1997). Depth dependence of earthquake frequency-magnitude distributions in California: Implications for rupture initiation. *Journal of Geophysical Research: Solid Earth*, *102*(B7), 15081–15090. https://doi.org/10.1029/97JB01356Nazareth, J. J. (2004). The Seismogenic Thickness of the Southern California Crust. *Bulletin of the Seismological Society of America*, *94*(3), 940–960. https://doi.org/10.1785/0120020129Papadopoulos, G. a., Charalampakis, M., Fokaefs, A., & Minadakis, G. (2010). Strong foreshock signal preceding the

L'Aquila (Italy) earthquake (Mw 6.3) of 6 April 2009. *Natural Hazards and Earth System Science*, *10*(1), 19–24. https://doi.org/10.5194/nhess-10-19-2010Petruccelli, A., Vannucci, G., Lolli, B., & Gasperini, P. (2018). Harmonic Fluctuation of the Slope of the Frequency–Magnitude Distribution (b-Value) as a Function of the Angle of Rake. *Bulletin of the Seismological Society of America*, *108*(4), 1864–1876. https://doi.org/10.1785/0120170328Petruccelli, A., Gasperini, P., Tormann, T., Schorlemmer, D., Rinaldi, A. P., Vannucci, G., & Wiemer, S. (2019). Simultaneous Dependence of the Earthquake-Size Distribution on Faulting Style and Depth. *Geophysical Research Letters*, *46*(20), 11044–11053. https://doi.org/10.1029/2019GL083997Ross, Z. E., Ben-Zion, Y., White, M. C., & Vernon, F. L. (2016). Analysis of earthquake body wave spectra for potency and magnitude values: implications for magnitude scaling relations. *Geophysical Journal International*, *207*(2), 1158–1164. https://doi.org/10.1093/gji/ggw327Scholz, C. H. (1968). Mechanism of creep in brittle rock. *Journal of Geophysical Research*, *73*(10), 3295–3302. https://doi.org/10.1029/JB073i010p03295Scholz, C. H. (2015). On the stress dependence of the earthquake b value. *Geophysical Research Letters*, *42*(5), 1399–1402. https://doi.org/10.1002/2014GL062863Schorlemmer, D., Wiemer, S., & Wyss, M. (2005). Variations in earthquake-size distribution across different stress regimes. *Nature*, *437*(7058), 539–542. https://doi.org/10.1038/nature04094Simpson, R. W. (1997). Quantifying Anderson's fault types. *Journal of Geophysical Research: Solid Earth*, *102*(B8), 17909–17919. https://doi.org/10.1029/97JB01274Spada, M., Tormann, T., Wiemer, S., & Enescu, B. (2013). Generic dependence of the frequency-size distribution of earthquakes on depth and its relation to the strength profile of the crust. *Geophysical Research Letters*, *40*(4), 709–714. https://doi.org/10.1029/2012GL054198Staudenmaier, N., Tormann, T., Edwards, B., Deichmann, N., & Wiemer, S. (2018). Bilinearity in the Gutenberg-Richter Relation Based on ML for Magnitudes Above and Below 2, From Systematic Magnitude Assessments in Parkfield (California). *Geophysical Research Letters*, *45*(14), 6887–6897. https://doi.org/10.1029/2018GL078316Staudenmaier, N., Tormann, T., Edwards, B., Mignan, A., & Wiemer, S. (2019). The frequency-size scaling of non-volcanic tremors beneath the San Andreas Fault at Parkfield: Possible implications for seismic energy release. *Earth and Planetary Science Letters*, *516*(June), 77–107. https://doi.org/10.1016/j.epsl.2019.04.006Trugman, D. T., & Shearer, P. M. (2017). GrowClust: A Hierarchical Clustering Algorithm for Relative Earthquake Relocation, with Application to the Spanish Springs and Sheldon, Nevada, Earthquake Sequences. *Seismological Research Letters*, *88*(2A), 379–391. https://doi.org/10.1785/0220160188Udias, A. (1999). Principles of Seismology. Cambridge University Press.Utsu, T. (1965). A method for determining the value of b in a formula logN=a-bM showing the magnitude-frequency relation for earthquakes. *Geophysical Bulletin of the Hokkaido University*, *13*, 99–103. Retrieved from http://hdl.handle.net/2115/13887Wiemer, S., & Wyss, M. (2002). Mapping spatial variability of the frequency-magnitude distribution of earthquakes. In *Advances in Geophysics* (Vol. 45, pp. 259–V).

https://doi.org/10.1016/S0065-2687(02)80007-3Woessner, J., & Wiemer, S. (2005). Assessing the Quality of Earthquake Catalogues: Estimating the Magnitude of Completeness and Its Uncertainty. *Bulletin of the Seismological Society of America*, *95*(2), 684–698. https://doi.org/10.1785/0120040007Wu, Y.-M., Chen, S. K., Huang, T.-C., Huang, H.-H., Chao, W.-A., & Koulakov, I. (2018). Relationship Between Earthquake b -Values and Crustal Stresses in a Young Orogenic Belt. *Geophysical Research Letters*, *45*(4), 1832–1837. https://doi.org/10.1002/2017GL076694Wyss, M. (1973). Towards a Physical Understanding of the Earthquake Frequency Distribution. *Geophysical Journal International*, *31*(4), 341–359. https://doi.org/10.1111/j.1365-246X.1973.tb06506.xYang, W., & Hauksson, E. (2013). The tectonic crustal stress field and style of faulting along the Pacific North America Plate boundary in Southern California. *Geophysical Journal International*, *194*(1), 100–117. https://doi.org/10.1093/gji/ggt113Yang, W., Hauksson, E., & Shearer, P. M. (2012). Computing a Large Refined Catalog of Focal Mechanisms for Southern California (1981-2010): Temporal Stability of the Style of Faulting. *Bulletin of the Seismological Society of America*, *102*(3), 1179–1194. https://doi.org/10.1785/0120110311